Sub-Nanometer Au Monolayer-Protected Clusters Exhibiting Molecule-like Electronic Behavior: Quantitative High-Angle Annular Dark-Field Scanning Transmission Electron Microscopy and Electrochemical Characterization of Clusters with Precise Atomic Stoichiometry

Laurent D. Menard,[†,‡] Shang-Peng Gao,[§] Huiping Xu,[§] Ray D. Twesten,[‡] Amanda S. Harper,[||] Yang Song,[||] Gangli Wang,[||] Alicia D. Douglas,[||] Judith C. Yang,[§] Anatoly I. Frenkel,[⊥] Ralph G. Nuzzo,*[,†,‡] and Royce W. Murray*[,||]

School of Chemical Sciences and Frederick Seitz Materials Research Laboratory, University of Illinois at Urbana−Champaign, Urbana, Illinois, 61801, Department of Materials Science and Engineering, University of Pittsburgh, Pittsburgh, Pennsylvania 15261, Kenan Laboratories of Chemistry, University of North Carolina at Chapel Hill, Chapel Hill, North Carolina, 27599, and Department of Physics, Yeshiva University, New York, New York 10016

Received: February 3, 2006; In Final Form: April 18, 2006

The synthesis and characterization of the clusters $Au_{13}[PPh_3]_4[S(CH_2)_{11}CH_3]_2Cl_2$ **(1)** and $Au_{13}[PPh_3]_4[S(CH_2)_{11}CH_3]_4$ **(2)** are described. These mixed-ligand, sub-nanometer clusters, prepared via exchange of dodecanethiol onto phosphine-halide gold clusters, show enhanced stability relative to the parent. The characterization of these clusters features the precise determination of the number of gold atoms in the cluster cores using high-angle annular dark-field scanning transmission electron microscopy, allowing the assignment of 13 gold atoms (±3 atoms) to the composition of both cluster molecules. Electrochemical and optical measurements reveal discrete molecular orbital levels and apparent energy gaps of 1.6−1.7 eV for the two cluster molecules. The electrochemical measurements further indicate that the $Au_{13}[PPh_3]_4[S(CH_2)_{11}CH_3]_2Cl_2$ cluster undergoes an overall two-electron reduction. The electrochemical and spectroscopic properties of the two Au_{13} cluster molecules are compared with those of a secondary synthetic product, which proved to be larger Au thiolate-derivatized monolayer-protected clusters with an average core of Au_{180}. The latter shows behavior fully consistent with the adoption of metallic-like properties.

Introduction

Metal nanoparticles have elicited much attention due to their interesting optical, electronic, chemical, and catalytic properties.[1−4] The complexity that emerges as metal particles become smaller in size—whether in terms of their atomic or electronic structures—can be quite substantial, however, which in turn poses challenges for developing predictive structure−property correlations for these systems. As metal particles decrease to sizes less than a few nanometers, their electronic properties transition from the bulk continuum of states to discrete molecular orbital energy levels.[5,6] In addition, structural habits that are not present in the bulk metal (e.g., transitions from close-packed to icosahedral motifs) may emerge.[7,8] Finally, the ligands or supports necessary to stabilize against particle aggregation and sintering will also come to play a more important role in determining the structural and chemical properties of the system.[9−13]

Size-dependent property correlations, while of considerable interest and an opportunity for research, are frequently limited by the availability of synthetic procedures that can yield metal clusters with widely variable but still discrete core sizes.[2,14] For this reason, the "bottom-up" chemical syntheses of ligand-protected metal and semiconductor nanoparticles have been of extreme interest in recent years.[10,15−28] A popular method used to prepare and stabilize gold nanoparticles in solution is the reduction of gold salts in the presence of phosphines or thiols, which form ligand shells around the metal cores. Phosphine-protected clusters can often be crystallized, yielding discrete cluster molecules with gold cores of 6, 8, 9, 10, 11, 13, 39, and 55 atoms being reported.[29−34] They are generally sensitive to oxidation, however, which can be problematic for their characterization and postsynthetic manipulation.[22] More recently, the report of Brust et al. demonstrated the facile synthesis of gold nanoparticles protected by monolayers of alkanethiolates.[15,16] These monolayer-protected clusters (MPCs) are quite stable under ambient conditions, can be protected with a wide variety of functionalized thiolates, are robust enough to survive further chemical derivatizations, and can be synthesized conveniently with average core diameters ranging between 1.1 and 9 nm.[17−21,35] The production of samples that are monodisperse in size, however, typically requires extensive postreaction ripening or fractionation.[18−21,23,24] The direct synthesis of thiolate-protected MPCs with core sizes less than 1 nm in size has been problematic.[28]

Recently, Hutchison et al. and others have demonstrated the exchange of thiols onto phosphine-halide clusters.[10,22,25−28,36,37] This technique results in exchange products protected by a mixed-ligand shell or fully thiolate-based monolayer. The core

* Authors to whom correspondence should be addressed. E-mail: r-nuzzo@uiuc.edu; rwm@unc.edu;
[†] School of Chemical Sciences, University of Illinois, Urbana.
[‡] Frederick Seitz Materials Research Laboratory, University of Illinois, Urbana.
[§] University of Pittsburgh.
[||] University of North Carolina, Chapel Hill.
[⊥] Yeshiva University.

10.1021/jp060739g CCC: $33.50
Published on Web 06/09/2006

size of the starting phosphine-halide cluster is sometimes retained, thus enabling the synthesis of highly monodisperse, stable nanoparticles.[10,22,26−28]

This report describes the synthesis and physicochemical properties of materials related to this class of ultrasmall MPCs prepared via thiol exchange onto phosphine-halide clusters. Through the use of a modification of the protocol described by Hutchison, two different sub-nanometer, gold cluster compounds were prepared that showed identical Au core atom counts but markedly different electrochemical and spectroscopic properties.[26] We describe the scope and use of an extremely powerful analytical technique—quantitative high-angle annular dark-field scanning transmission electron microscopy (HAADF−STEM)—to determine the atomic compositions of these Au nanoparticle cores and confirm their monodisperse natures. The sensitivity of the electronic properties of nanometer-sized ligand-protected metal particles to slight changes in core size and structure, as well as to ligand stoichiometries, requires precise characterization of these quantities. In the former case, the determination of apparent core diameters in electron micrographs is insufficient to distinguish between cluster materials that differ by only a few metal atoms in their cores, highlighting a need to develop techniques that can directly characterize single clusters on the basis of their atomic structures.[38−42] In some instances, cluster samples can be crystallized and characterized using single-crystal X-ray diffraction, yielding not only a precisely determined stoichiometry but also the structure of the cluster core and ligand shell with which electronic properties can be correlated.[8,32,33,43,44] Many metal nanoparticles of recent interest, however, have not been successfully crystallized, in many cases because they exist as polydisperse samples possessing distributions of molar mass.[14] Mass spectrometry has shown promise for the determination of cluster core size distributions, but its application is not without difficulty, and it is inapplicable for systems stabilized by solid supports.[14,45−48]

The present work demonstrates the use of a mass-sensitive method that can be used to characterize the core compositions of nanoparticles on a single cluster basis, whether stabilized by ligands or solid supports. The HAADF−STEM technique, also known as *Z*-contrast microscopy, collects the high-angle (>100 mrad), incoherently scattered electrons on an annular detector.[39−42,49,50] The advantage of detection in this mode is twofold. First, at these angles the ratio of high-*Z*/low-*Z* electron scattering cross sections is greater than that at low angles, improving contrast between the gold cluster cores and the supporting low-*Z* substrate.[50] Second, the detected scattering is largely of the Rutherford type, and Bragg diffracted electrons are excluded, resulting in a signal per cluster that is proportional to the number of gold atoms in the cluster core and that is quantifiable as such.[39−42] Using this methodology, we were able to verify the 13 atom gold cluster core compositions of the two cluster molecules $Au_{13}[PPh_3]_4[S(CH_2)_{11}CH_3]_2Cl_2$ **(1)** and $Au_{13}[PPh_3]_4[S(CH_2)_{11}CH_3]_4$ **(2)**. The ligand shell differences in **1** and **2** engender significant variations in spectroscopic and electrochemical properties that we correlate and compare with a polydisperse sample of larger (and more commonly studied) MPCs with an average core of ∼180 Au atoms. The data reveal the molecular natures of the Au_{13} clusters and the metallic nature of the Au_{180} MPCs.

Experimental Methods

Materials. Hydrogen tetrachloroaurate hydrate (Strem Chemicals, 99.9%), sodium borohydride (Acros, 98%), 1-dodecanethiol (98%, Aldrich), triphenylphosphine (99%, Aldrich), and all solvents were used as received. Water was purified with a Millipore Milli-Q system (18.2 MΩ cm).

$Au_{13}[PPh_3]_4[S(CH_2)_{11}CH_3]_2Cl_2$ (1). Mixed-ligand Au_{13} clusters were prepared using a variation of a literature procedure in which a phosphine-halide cluster was prepared (but not isolated) and directly reacted with dodecanethiol.[26] Briefly, 500 mg (1.5 mmol) of $HAuCl_4$ was dissolved in 100 mL of tetrahydrofuran (THF). To this stirring solution was added 3 mmol of PPh_3. The solution was reduced by dropwise addition of 30 mL of ethanolic 0.15 M $NaBH_4$ solution over 30 min. To the reaction mixture was added 4.5 mmol of dodecanethiol, and the solution was allowed to stir for 24 h at room temperature. The solution was washed once with water, and the solvent was removed from the organic fraction under vacuum (25 °C). The solid material was then dissolved in 200 mL of *n*-pentane and transferred to a separatory funnel. The solution was extracted with 100-mL portions of acetonitrile until the acetonitrile layer was colorless. The acetonitrile was removed under vacuum, and the solid was dissolved in a minimum amount of 2-propanol. The crude product was loaded on a silica gel column (mobile phase 3:1 2-propanol/toluene). The late eluting brown band was collected, and the solvent was removed under vacuum. Typical yields were 80−100 mg (17−22% Au).

$Au_{13}[PPh_3]_4[S(CH_2)_{11}CH_3]_4$ (2). The synthesis described above was followed with the exception that an excess of $NaBH_4$ (30 mL of 0.45 M $NaBH_4$) was added to ensure full reduction of chloro(triphenylphosphine)gold(I) *and* neutralization of HCl. After the aqueous wash and removal of organic solvents the solid was dissolved in ca. 100 mL of 2-propanol and filtered through a medium glass frit to remove insoluble products and larger colloids. The 2-propanol was removed under vacuum. The solid product was then purified on a silica gel column (mobile phase 2:1 toluene/2-propanol). The product eluted last off the column as a broad brown band was collected, and the solvent was removed under vacuum. The product slowly decomposes under an ambient atmosphere and was therefore stored under nitrogen to prevent oxidative decomposition.

Fully Thiolated Au MPCs. A secondary product that proved to be larger, fully thiolated MPCs was obtained from the protocols described above. In either of the two syntheses described above, the first band off the column (brown in color) was collected, and the solvent was removed. The solid was dissolved in a minimal amount of pentane and transferred to centrifuge tubes. A 20-fold excess of acetone was then added, which resulted in the precipitation of a black solid. The samples were centrifuged at 3000*g*, and the supernatant was decanted. Dissolution in *n*-pentane followed by precipitation with acetone and centrifugation was repeated several times to yield the purified product.

Characterization. ^1H and $^{31}P\{H\}$ NMR spectra were recorded on a Varian Unity 400 MHz high-resolution Fourier transform NMR spectrometer using acetone-d_6 or $CDCl_3$ as solvents. $^{31}P\{H\}$ spectra were referenced using an external standard of 85% H_3PO_4. UV−vis spectra, in the region 250−900 nm, were collected on methylene chloride cluster solutions using a Varian Cary 5 G spectrophotometer. X-ray photoelectron spectra were acquired using a Kratos Axis ULTRA X-ray photoelectron spectrometer with a monochromatic Al Kα source and a hemispherical analyzer positioned at a takeoff angle of 54.7°. The samples were prepared by dropping a toluene solution of nanoparticles onto a piece of silicon wafer to form a thin film. Binding energies were referenced to adventitious carbon (284.8 eV).

Electrochemistry. Electrochemical analysis was performed with a CH Instruments model 650B electrochemical workstation using a platinum working electrode (diameter 1.6 mm), a platinum wire auxiliary electrode, and a Ag/Ag^+ reference electrode in an electrolyte solution of 0.1 M tetrabutylammonium perchlorate (TBAP) in dichloromethane. Solutions were measured at room temperature or at −78 °C (acetone/dry ice bath).

Near-Infrared Luminescence. UV−visible spectra were collected with a Shimadzu UV−vis (model UV-1601) spectrometer. Photoluminescence spectra were taken in a 90° geometry on a modified Jobin Yvon Fluorolog FL321 spectrometer with a 450 W xenon source. The spectrometer was equipped with two detectors, a Hamamatsu R928 photomultiplier tube (visible wavelengths) and InGaAs (near-IR wavelengths, connected via a T channel). Dilute solutions, to minimize the influence of self-absorbance and self-quenching, were freshly prepared before measurements. Methylene chloride was used as the solvent. Emission spectra were taken with excitation at 450 nm for visible wavelengths and 400 and 680 nm for near-IR wavelengths. Quantum yields were measured with respect to 3,3′-diethylthiatricarbocyanine iodide (DTTC).

High-Performance Liquid Chromatography. A Waters 600 controller pump capable of gradient elution was used for high-performance liquid chromatography (HPLC) with a Waters 996 PDA detection system. Injection was performed through a Rheodyne 7725 injection valve with a 50 μL loop. For higher-resolution separations,[51] two stainless steel columns with different packing materials were utilized in line. The stationary phase in the first column (250 mm × 4.6 mm i.d.) was silica-bonded C8 with a pore size of 120 Å (Thermo Hypersil, Keystone Scientific Operations), and that in the second one (150 mm × 4.6 mm i.d.) was silica-bonded phenyl with a pore size of 5 μm (Shandon HPLC Co.). The mobile phase flow rate was set at 0.7 mL/min, and the column temperature was set at 30 °C. The mobile phase consisted of dichloromethane with 10 mM tetrabutylammonium perchlorate.

Electron Microscopy. Electron microscopy was used to determine cluster particle diameters and provide atomic counting by the quantitative HAADF−STEM method. Acetone or toluene solutions of the Au cluster compounds were cast onto TEM grids with an ultrathin carbon film (Ted Pella, Inc.). Quantitative HAADF−STEM experiments were performed on a field-emission, Vacuum Generators HB501 STEM operated at 100 kV. Images were acquired at 1M× magnification, and the image size was 1024 × 1024 pixels, yielding a pixel dimension of 0.62 Å. This sampling size was sufficiently small in comparison to the particle size (8 Å) and the probe size (∼1 nm) to minimize intensity errors from undersampling as described in previous work.[39] The exposure time used was 64 μs/pixel. For the collection of annular dark-field images the detector was masked resulting in an inner collection angle of 130 mrad. The outer angle of collection (520 mrad) was defined by the outer diameter of the ADF detector and by postspecimen compression affected by the objective lens settings.[52] With each particle image, an accompanying image was taken to measure the signal from the carbon film substrate alone.

The electron beam current was measured after image acquisition using a collector aperture lying along the electron−optic axis of the microscope. A Keithley analogue electrometer capable of measuring picoampere currents was used.

To calibrate the ADF detector, the image of the detector was recorded in selected area diffraction mode with the electron beam current reduced by a factor of ∼100 to prevent saturation of the detector but otherwise under the same conditions as during sample imaging. The detector does not show a uniform response but instead shows an angular dependence on the number of counts with the more damaged inner detector regions showing lower counts than the higher-angle regions (data provided as Supporting Information). Dark counts (taken as the counts detected in the mask region) were subtracted from the profile to yield the ideally zero response at the mask surface. The profiles of 30 rays originating from the center of the detector were averaged to yield the number of counts as a function of scattering angle, $N_0^{\text{low}}(\Theta)$ where the superscript "low" refers to the attenuated current used to image the detector and Θ is the scattering angle. The detector angles of collection were calibrated by imaging a standard sample of large Au nanoparticles in selected area diffraction mode under the same conditions as the ADF detector image acquisition and referencing the images to the {220}and {311} rings of the Au particles. The detector response must also be normalized by the atomic scattering cross sections since the scattered intensity falls off as a function of scattering angle. Consequently, contributions from higher angles contribute less to the measured intensity despite the higher sensitivity of the detector at these angles. The normalized detector counts for the dark-field images of the particles are given by the equation

$$N_0^{\text{high}} = \left(\frac{\sum_{\Theta=\beta_{\min}}^{\Theta=\beta_{\max}} N_0^{\text{low}}(\Theta) f(\Theta)^2 \, 2\pi \sin\Theta \, d\Theta}{\sum_{\Theta=\beta_{\min}}^{\Theta=\beta_{\max}} f(\Theta)^2 \, 2\pi \sin\Theta \, d\Theta} \right) \left(\frac{I_{\text{high}}}{I_{\text{low}}} \right) \quad (1)$$

where $\beta_{\min}$ is the inner detector angle (130 mrad), $\beta_{\max}$ is the outer detector angle (520 mrad), $N_0^{\text{low}}(\Theta)$ is the detector response at the attenuated current, $f(\Theta)$ is the atomic electron scattering factor of gold, I_{high} is the current of the electron beam used to image the particles, and I_{low} is the attenuated beam current used to image the detector for calibration.[39,40] The scattering factor of gold was used although the normalization factor is not element-specific because at the high detection angles used in these measurements the scattering is Rutherford-type and the element-specific terms cancel in the normalization ratio.[39] The determination of the angle-dependent scattering factor is described below.

Particle diameters were determined in the Gatan Digital Micrograph software package by plotting the intensity profiles across individual particles and measuring the full width at half-maximum (fwhm). Particle intensities were measured by first subtracting the background scattering from the carbon substrate from the corresponding particle image. The integrated particle signal was determined using Digital Micrograph by drawing a circle around the individual particle and integrating the intensity in this area. The absolute cross section, σ_{cluster} (Å^2), of the particle is given by the expression

$$\sigma_{\text{cluster}} = T_{\text{int}} \left(\frac{\Delta^2}{N_0^{\text{high}}} \right) \quad (2)$$

where T_{int} is the integrated intensity measured from the image and Δ^2 is the pixel area (Å^2).[39,40] The ratio on the equation right-hand side is the inverse of the incident current density on the particles.[39]

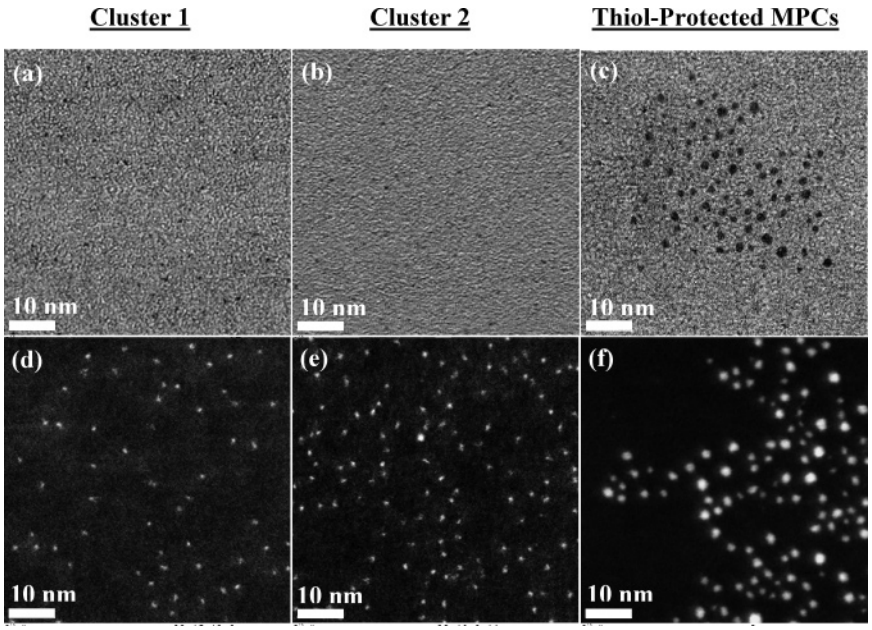

Figure 1. Representative BF−STEM images of (a) **1**, (b) **2**, and (c) thiol-protected MPCs. Representative HAADF−STEM images of (d) **1**, (e) **2**, and (f) thiol-protected MPCs. All images collected at 1 M× magnification. Parts a and d are images of the same area collected simultaneously. Parts b and e are images of different areas on the TEM grid, as are c and f.

Results and Discussion

Electron Microscopy. Figure 1 shows representative bright-field (BF) STEM images for samples of clusters **1** and **2** and the fully thiolated MPCs (Figures 1a, 1b, and 1c, respectively). The micrographs illustrate the low contrast between the gold nanoparticles (because of their very small size) and the ultrathin carbon film substrate. In the case of the sub-nanometer gold clusters, the particles are barely distinguishable against the background. Figures 1d−f are representative HAADF−STEM micrographs of these same materials. The latter images show much greater contrast between the high-*Z* gold particles and the low-*Z* carbon support. All images shown in Figure 1 were recorded at 1M× magnification.

As noted in the Experimental Section, the number of atoms in the cluster cores can be determined by dividing the measured cluster scattering cross section by the theoretical atomic scattering cross section. The atomic scattering cross section is calculated using a partial-wave method.[39,40] The electron scattering factor, $f_e(\Theta)$ is calculated using the Mott Formula

$$f_e(\Theta) = \frac{m_0 e^2}{8\pi h^2 \varepsilon_0}\gamma\left(\frac{\lambda}{\sin(\Theta/2)}\right)^2 (Z - f_x(\Theta)) \qquad (3)$$

where m_0 is the rest mass of the electron, e is the electron charge, h is Planck's constant, ε_0 is the vacuum permittivity, γ is a relativistic correction factor ($\gamma = (1 - v^2/c^2)^{1/2}$, v is the electron velocity and c is the speed of light in a vacuum), λ is the electron wavelength at 100 kV (0.037 Å), Z is the atomic number, and $f_x(\Theta)$ is the atomic X-ray scattering factor.[39]

The X-ray scattering factor is determined by the analytical expression

$$f_x(k) = \sum_{i=1}^{4} a_i \exp(-b_i k^2) + c \qquad (4)$$

with the coefficients a_i, b_i, and c given in the International Tables of X-ray Crystallography and $k = \sin(\Theta/2)/\lambda$.[53] The electron scattering cross section for gold atoms over the scattering angles measured in these experiments ($\beta_{min} = 130$ mrad, $\beta_{max} = 520$ mrad) was calculated from the formula[40]

$$\sigma_e(\beta_{min},\beta_{max}) = \sum_{\Theta=\beta_{min}}^{\Theta=\beta_{max}} |f_e(\Theta)|^2\, 2\pi \sin\Theta\, d\Theta \qquad (5)$$

The electron scattering cross section for a single gold atom was calculated to be 0.0185 Å^2.

Figure 2 shows the experimental measurements from the HAADF micrographs for **1**, **2**, and the fully thiolated MPCs with the number of core atoms plotted versus the particle diameter. Presentation of the data in this form is particularly useful as it provides a deterministic measurement of the three-dimensional shape of the cluster cores.[38,42] Included in the plots are profiles for models of clusters with spherical, hemispherical, or monolayer (111) island-type structures. The Au_{13} clusters (cluster **1** and cluster **2**) exhibit apparent spherical core geometries as shown by the agreement of the average values of core atoms and diameter solely with this structural model and not those for the hemispherical and monolayer island motifs. In the case of the thiolate-protected MPCs (and in contrast to the Au_{13} clusters) there is a broad, non-Gaussian distribution of cluster sizes. To properly depict this dispersity, the number of core atoms for each individual particle is plotted against its diameter. For this sample, the agreement with a spherical core model is consistent over a wide range of cluster sizes.

The narrow distribution in the core composition of the Au_{13} cluster molecules is immediately evident through comparison with the thiolate-protected MPC distribution. The particle sizes are determined to be 0.8 ± 0.1 nm for samples of clusters **1** and **2**. This result is consistent with the earlier reports of ligand exchange on Au_{11} phosphine-halide clusters.[10,26] In those studies, retention of the Au_{11} core was assumed since there was no obvious change in core size after thiol exchange onto the parent cluster. The loss or gain of a small number of atoms in the cluster core, however, cannot be detected by simply measuring the cluster diameter. The fully thiolated MPCs show a size distribution with an average size of 2.0 ± 0.5 nm. Particles of this size are commonly prepared via the Brust synthesis and

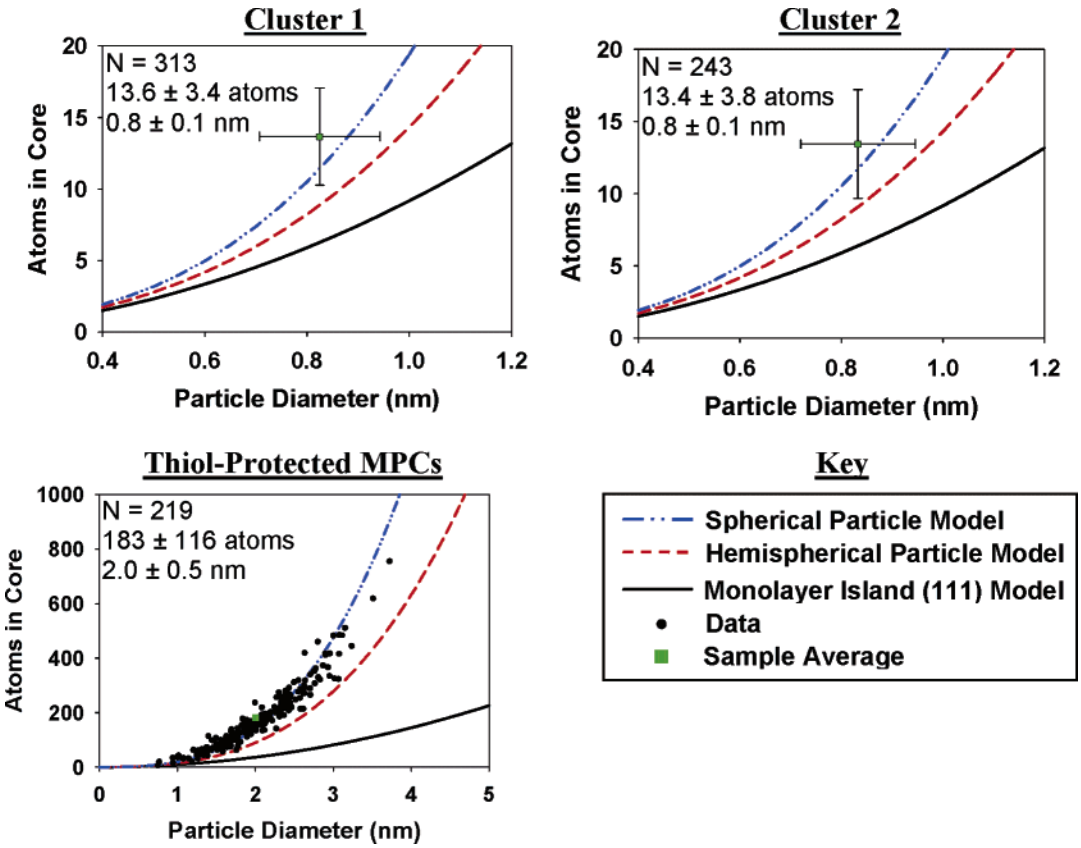

Figure 2. Core atom counts for gold clusters measured using the quantitative HAADF−STEM technique for **1**, **2**, and thiolate-protected MPCs, respectively, plotted against measured particle diameters. The dependence of core atoms on particle diameter is compared to the theoretically determined dependencies of spherical particles, hemispherical particles, and (111) close-packed monolayer islands. Clusters **1** and **2** are presented as the average measurements for each sample with uncertainties, whereas presentation of each individual particle measured in the polydisperse sample of thiolate-protected MPCs is more illustrative of the correlation of particle diameter and number of core atoms.

are consistent with cores containing an estimated average of ca. 200 gold atoms.[54]

Cluster **1** shows a distribution in measured core atoms centered at 13.6 atoms with an uncertainty of ±3.4 atoms (25%). Cluster **2** shows a similar result of 13.4 ± 3.8 atoms. As described below, the uncertainties in these measurements of the Au_{13} clusters are estimated to be largely due to experimental errors, and the narrow distributions reported are evidence of cluster molecules with very little distribution in gold core composition. In contrast to the narrow distributions of the sub-nanometer cluster molecules, the larger thiolate-protected MPCs display a larger distribution in the number of atoms in the core, consistent with the distribution in core sizes. The average number of atoms in the core is 183 atoms with a standard deviation of 116 atoms. The latter value, given how large it is compared to the 3 atom uncertainty of the HAADF−STEM measurement (see below), demonstrates the marked heterogeneity of the latter MPC sample.

The background subtraction procedure requires the imaging of both the gold particles and an out-of-focus region of the carbon film substrate, subtracting the latter from the former. This method presumably minimizes the systematic errors in the measurement, since the instrument and data acquisition settings do not change appreciably between the two acquisitions. The validity of this background subtraction protocol was separately evaluated by measuring the signal intensity in several hundred areas of the background subtracted images where no particles were present. The intensity distribution so determined was centered on zero.

Sources of random error in the measurements include variations in the carbon substrate thickness. This source is believed to make the largest contribution to measurement errors. This is evident immediately in the context of the 3 atom uncertainty of the HAADF−STEM measurement. To provide an estimate of the contribution of instrumental error to the total uncertainty, the particle analysis routine was performed on over 100 areas of the carbon support where no gold particles were present. The mean calculated number of gold atoms for this sample set was zero (7.5×10^{-5}), as expected, but the standard deviation in the measured scattering cross section (±0.058 Å^2) corresponded to deviations equivalent to ±3.1 gold atoms in the particle measurements. By subtraction of the variance of the carbon film measurements from the variance of the particle measurements, the contribution of other sources of error for the Au_{13} clusters (including actual distribution in the cluster core composition) is estimated to be ca. ±1 atom. Errors can also result from the presence of the organic ligands protecting the clusters, the slight contribution of coherent scattering to the measured intensity, and specimen drift during the measurement.[40] They are expected to be negligible in this case.

A concern in electron microscopic studies of small metal particles is the possibility of particle sintering caused by electron beam irradiation.[55] The stability of the specimens was therefore assessed by monitoring a single area on the sample grid for over an hour while under illumination by the electron beam. The carbon-supported samples were found to be very stable, not showing any significant diffusion on the substrate surface or particle sintering despite the fact that exposure to an electron

TABLE 1: Elemental Compositions Determined from Quantitation of the High-Resolution X-ray Photoelectron Spectra

sample	Au	S	P	Cl
1	13	2.0	4.1	1.6
2	13	3.7	3.6	0.6
thiolate-protected MPCs	183	40	5	0

beam is known to remove the clusters' protective organic ligands.[56,57]

X-ray Photoelectron Spectroscopy. The stoichiometry of the ligand shell was determined from the elemental ratios measured by X-ray photoelectron spectroscopy (XPS). Since the cluster size is similar to or less than photoelectron escape depths, XPS gives a good average response to overall composition.[17] In addition, the ability to analyze different chemical states is desirable in confirming sample purity and detecting subtle differences in the oxidation state of the Au_{13} cluster cores.

The elemental compositions determined from the quantification of high-resolution X-ray photoelectron spectra are presented in Table 1. The gold composition in the table was set to the average number of atoms in the nanoparticle cores as determined from the HAADF−STEM measurements. We note that given the uncertainty of ca. ±1 Au atom in the HAADF−STEM determination of Au cluster core stoichiometries the elemental compositions presented in Table 1 have correlated uncertainties of the same order or magnitude (i.e., ±10%).

The high-resolution Au 4f core level data provide insights as to the nature of the chemical states of the gold atoms present in the cluster core. The Au $4f_{7/2}$ peak for the fully thiolated MPCs appears at a binding energy of 84.0 eV and displays a narrow peak width (fwhm = 1.1 eV). These characteristics are essentially those of bulk gold, which suggests a metallic nature for the MPC core.[58] For the case of cluster **2**, the binding energy is also that of bulk gold (84.0 eV), and in the case of cluster **1** the binding energy is shifted to a slightly greater value of 84.4 eV. Both samples exhibit broader peak widths (fwhm = 1.5 eV) than the larger MPCs. Other cluster core levels scanned in high-resolution mode (P 2p, S 2p, Cl 2p, C 1s) did not show any broadening (as would be indicative of differential charging); broadening is observed solely in the Au 4f high-resolution spectra. The slightly higher binding energy for cluster **1** relative to the other two cluster samples may be a result of a partial positive charge on the 13 atoms of the gold core.[59] It should be noted, however, that binding energy shifts due to final state effects are also expected to be significant for small Au clusters.[60,61]

NMR Spectroscopy. We measured the ^1H and $^{31}P\{H\}$ NMR spectra for **1**, **2**, and the thiolate-protected MPCs. These data are provided as Supporting Information and summarized here. The main value of these data is the speciation it establishes of the organic ligand shells surrounding the various Au clusters. For the two Au_{13} clusters, the data strongly establish the presence of both bonded phosphine and thiolate ligands. For **1**, integration of the aromatic (δ = 6−8.5 ppm) and aliphatic (δ = 0.2−1.4 ppm) regions of the ^1H NMR spectrum reveals an aromatic/aliphatic ratio of 27:25 consistent with a 2:1 triphenylphosphine/dodecanethiolate ratio (ideally 30:25). For **2** the aromatic/aliphatic ratio is 17:25, approximately equivalent to a 1:1 triphenylphosphine/dodecanethiolate stoichiometry (ideally 15:25). These stoichiometric determinations are consistent with the results of independent XPS elemental quantifications. The latter data also strongly suggest facile ligand exchange processes occurring on the NMR time scale for this compound. This inference was strongly supported by the results of variable temperature $^{31}P\{H\}$ NMR data.

Whereas the $^{31}P\{H\}$ NMR spectra for **1** are characterized by a single, sharp resonance at δ = 50 ppm, that for **2** is a broadened signal observed in the range δ = 44−52 ppm. The presence of a single sharp peak in the $^{31}P\{H\}$ NMR spectra of **1** is indicative of Au−P bonding at equivalent (or nearly equivalent) gold-phosphine sites.[62] Addition of free triphenylphosphine does not result in any change in the peak shape or chemical shift, nor do low-temperature measurements show any change in shape or position, discounting fast ligand exchange as an explanation for a single sharp resonance.[52,63,64]

Variable temperature $^{31}P\{H\}$ NMR measurements confirm that the broad resonances seen for **2** result from ligand dynamics. Notably, the addition of an excess of triphenylphosphine to the cluster solution of **2** results in the emergence of the single sharp peak at δ = 50 ppm and a broadening of the triphenylphosphine resonance (δ = −6 ppm). Taken together, these data strongly assert that the ligand shells of the Au_{13} clusters contain both thiolate and phosphine ligands and that they differ in compounds **1** and **2**—both structurally and stoichiometrically.

High-Performance Liquid Chromatography. The STEM measurements presented above illustrate the narrow size distribution that characterizes the Au_{13} cluster molecules. The sample size in the microscopy provides good statistics, and imaging of a number of different areas on the TEM grid did not reveal any areas of larger particles that might result from size-selective segregation. The areas measured by electron microscopy are limited, however, and an ensemble measurement of nanoparticle distributions would be desirable. Recent work by several groups has advocated the use of chromatographic separations to analyze size dispersity in ligand-protected metal nanoparticles.[36,55,65−68] The use of both size-exclusion and HPLC has been demonstrated to this end, and HPLC is used here to further demonstrate the monodisperse nature of a sample of cluster **1**.

Figure 3 shows the HPLC chromatogram for **1**, which consists of a dominant peak at ca. 8 min. A small earlier eluting peak at 7.7 min is due to low-molecular-weight impurities (identified by ^1H and $^{31}P\{H\}$ NMR as being due to trace impurities of Ph_3PO and Ph_3PAuCl in this particular sample). UV−vis spectra were collected at various times along the peak and are included in Figure 3. The elution of a single, narrow peak and the measurement of identical UV−vis spectra across the width of the peak are indicative of a highly monodisperse sample. Chromatography of samples with a higher population of large clusters exhibited wider chromatographic peaks with UV−vis spectra that varied across the peak (data not shown). While HPLC operated under the conditions described here is effective at determining the presence of cluster **2** and the larger thiolate-protected MPCs in a sample of cluster **1**, its ultimate resolving power for distinguishing between clusters of this class that differ by one or two gold atoms in the cluster core is unknown. HPLC could be a valuable tool for such high-resolution measurements, however, because the stoichiometry of the ligand shell (and thus the polarity of the cluster) is expected to be highly sensitive to the number of Au core atoms for clusters in which a large percentage of the Au atoms are at the cluster surface.

UV−Visible Spectroscopy. UV−visible spectroscopy is widely used in the characterization of metal nanoparticles as a probe of their size-dependent electronic structure. Larger gold colloids (≥2 nm) display the well-known surface plasmon band at ca. 520 nm.[2,69] The intensity of this absorption band decreases with a decrease in cluster size in accordance with theory.[69] For

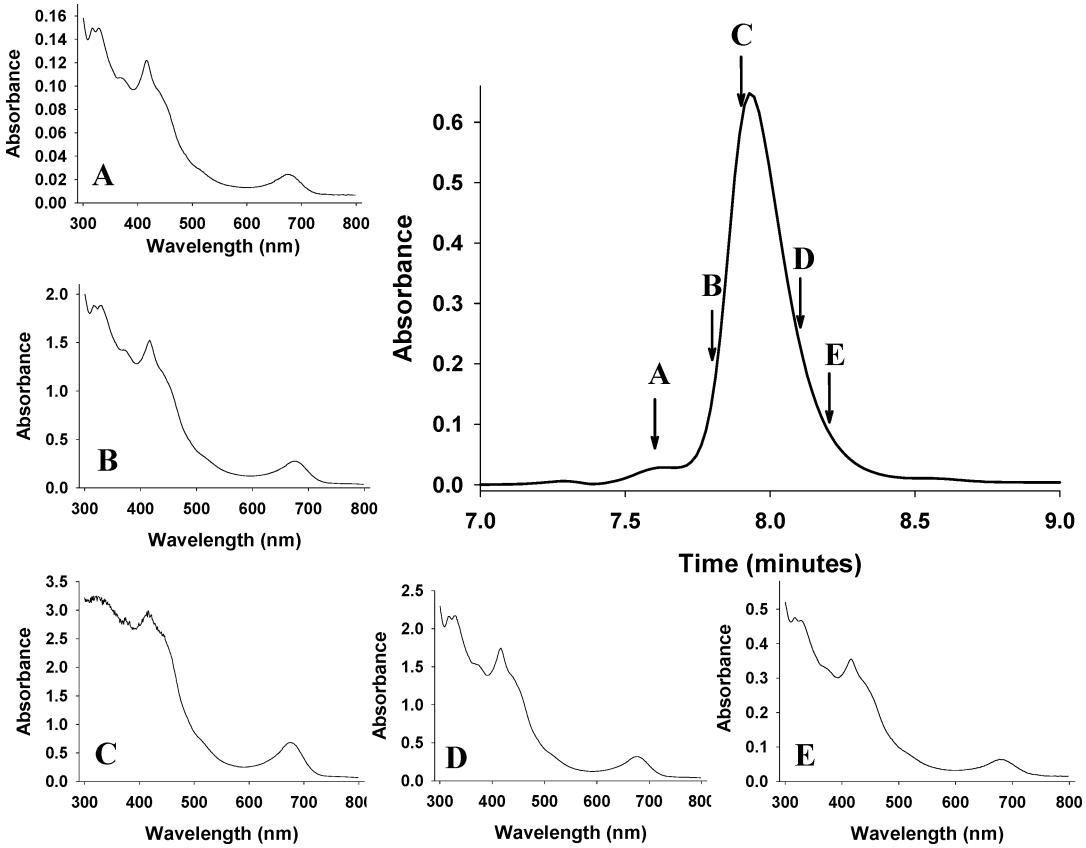

Figure 3. HPLC chromatogram of a sample of cluster **1** (detection at 520 nm) with full UV−vis spectra taken at (A) 7.6, (B) 7.8, (C) 7.9, (D) 8.1, and (E) 8.2 min. The greater noise at wavelengths <400 nm in spectrum C results from the high concentration in the center of the chromatographic peak.

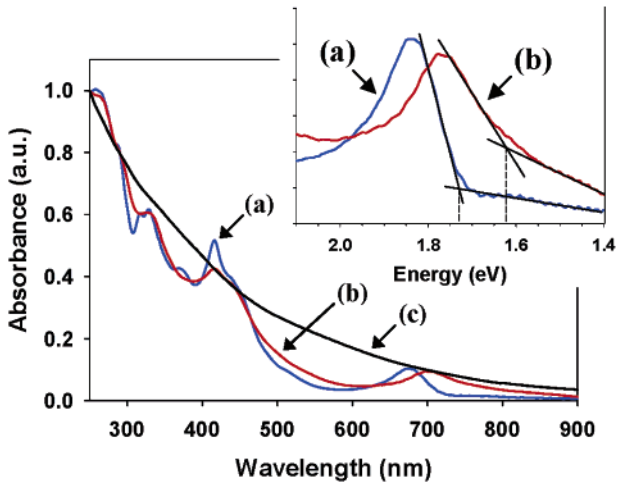

Figure 4. Normalized (at 250 nm) UV−vis spectra for (a, blue) **1**, (b, red) **2**, and (c, black) fully thiolated MPCs. The inset is plotted in electronvolts and shows the lowest-energy peaks and estimated energy gap.

the case of nanoparticles with diameters less than 2 nm, the surface plasmon resonance disappears completely, leaving a smooth spectrum with absorbance increasing exponentially from the visible to the ultraviolet region.[17,54] With a further decrease in size (nanometer to sub-nanometer), the emergence of discrete peaks in the UV−vis spectra is observed.[26,47,51,54,70] This marks a transition from a bulklike metallic density of states to an electronic structure described by discrete molecule-like electronic levels.

Figure 4 presents the UV−vis spectra for the three cluster samples. The thiolate-protected MPCs display a smooth exponential UV−vis spectrum (Figure 4c) characteristic of gold nanoparticles with diameters between 1.5 and 2 nm and a fairly polydisperse size distribution. Figures 4a and 4b are the spectra for **1** and **2**, respectively, which show discrete peaks indicative of molecule-like electronic levels but with some obvious differences in the spectral shape of the two samples. Similar spectra were obtained by Hutchison et al. and Chen et al. for samples of a reported fully thiolate-protected Au_{11} cluster.[10,26]

Spectra of clusters displaying such molecule-like transitions have been observed in a number of small nanoparticle systems, and reports suggest that they are highly sensitive to the cluster core size and geometry, ligand identity, and the effects of oxidation.[30,71−74] The onset of absorption involves a transition between the highest occupied molecular orbital (HOMO) and lowest unoccupied molecular orbital (LUMO) or nearby electronic levels.[21,74,75] The energy of this transition is generally estimated as the onset wavelength of absorption, λ_{onset}.[74] The estimated onset of absorption for the present Au_{13} systems (shown in the inset of Figure 4) is 1.73 eV (718 nm) for **1** and 1.63 eV (761 nm) for **2**. These wavelengths are in good agreement with the electrochemically determined energy gaps of 1.76 and 1.57 V (see below) for **1** and **2**, respectively. This strongly suggests that both the optical transitions and the electrochemical electron-transfer processes are probing the same cluster properties.

Electrochemistry. Electrochemical measurements provide a powerful means for exploring the properties of highly monodisperse semiconductor and metal nanoparticles, especially with regards to HOMO−LUMO energy gaps (as measured using the first oxidation and reduction peaks in differential pulse voltammograms or, equivalently, the $E_{1/2}$ potentials for these redox

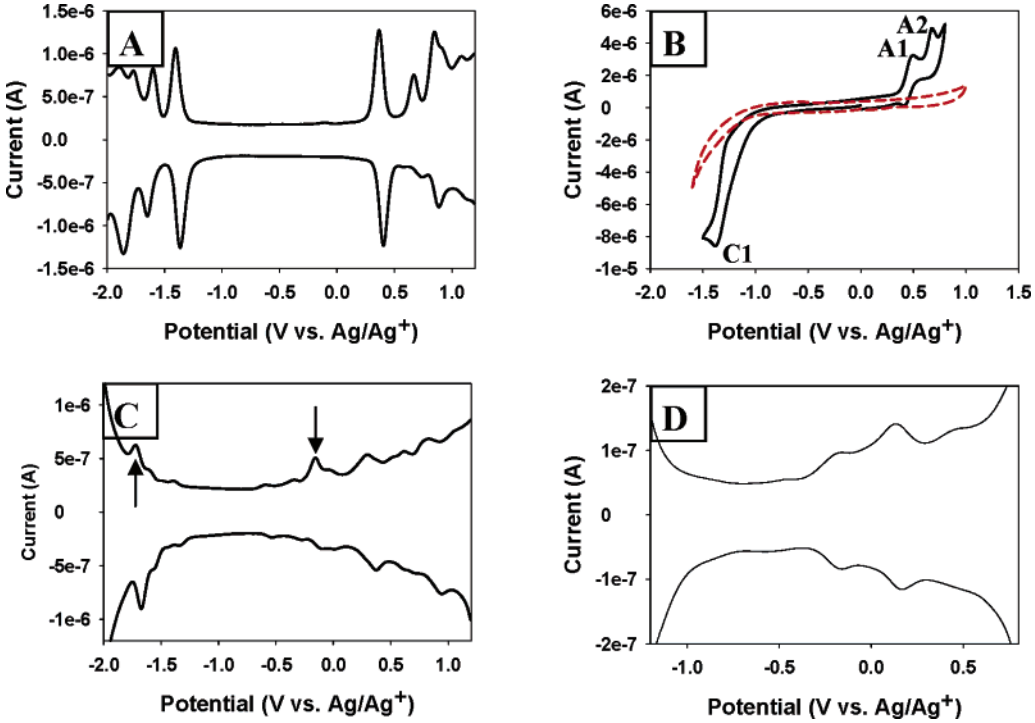

Figure 5. (A) Differential pulse voltammetry for **1** (−78 °C). (B) Cyclic voltammetry for **1** (25 °C) with the first (A1) and second (A2) anodic peaks and the cathodic (C1) peak labeled (see text). The dashed voltammogram is of the blank electrolyte solution. (C) Differential pulse voltammetry for **2** (−78 °C). The arrows indicate the peaks that delimit the electrochemical energy gap in the oxidative scan (see text). (D) Differential pulse voltammetry for larger, thiol-protected MPCs (25 °C). See text for details.

couples in cyclic voltammograms).[5,21,51,76,77] Yang and Chen presented electrochemical measurements of sub-nanometer gold clusters synthesized via thiol exchange onto the phosphine-halide cluster $Au_{11}(PPh_3)_7Cl_3$.[10] This material, assigned to a fully thiol-exchanged Au_{11} core, exhibited a good agreement between the electrochemically measured energy gap (1.76 V) and that measured optically (1.83 eV).[10]

Voltammetry studies of **1** were revealing in this regard, showing an electrochemical gap that is essentially identical to that reported previously for the Au_{11} cluster.[10] The differential pulse voltammograms presented in Figure 5A show increased detail relative to the earlier report due to the reduced temperature (−78 °C) of the sample solution.[10] The voltammograms consist of a large central gap delimited by the first oxidation and reduction peaks. At more negative (positive) potentials than the first reduction (oxidation) peak subsequent reductions (oxidations) are resolved. The electrochemically measured energy gap, taken as the difference between the potentials of the first reduction and oxidation peaks in the differential pulse voltammograms, yields a value of 1.76 V, similar to that deduced from the UV−vis spectroscopy data, 1.73 eV. The present data are noteworthy in this sense as the stiffly determined 13 atom count of the core of **1** leads us to believe that the earlier assignments may be in error.[10,26]

Room-temperature cyclic voltammetry (CV) of **1** (Figure 5B) provides additional information about the cluster molecule. The cathodic and anodic processes appear to be only partially reversible, consistent with possible chemical changes in the clusters upon reduction or oxidation. The cathodic peak at −1.4 V (C1) appears to correspond to a multiple-electron reduction since its peak current is approximately 3 times greater than the presumably one-electron oxidation peak currents at +0.5 eV (A1) and +0.7 eV (A2). The diffusion coefficient for the oxidation ($0 \rightarrow +1$) can be determined from the peak current from the equation

$$i_p = 0.4463\left(\frac{F^3}{RT}\right)^{1/2} n^{3/2} A D^{1/2} C^* \upsilon^{1/2} \qquad (6)$$

where i_p is the peak current (*A*), *F* is the Faraday constant (C mol^{-1}), *R* is the gas constant (J mol^{-1} K^{-1}), *T* is the temperature (K), *n* is the number of electrons transferred, *A* is the area of the electrode (cm^2), *D* is the diffusion coefficient of the cluster (cm^2 s^{-1}), C^* is the concentration of the cluster in the bulk (mol cm^{-3}), and υ is the sweep rate (V/s).[78] The diffusion coefficient of **1** thus calculated from peak A1 was found to be 1.9×10^{-6} cm^2 s^{-1}. The diffusion coefficient for the Au_{13} cluster is similar to those measured for Au_9, Au_{38}, and Au_{140} ligand-protected clusters.[24,79,80] A linear dependence of peak currents on $\upsilon^{1/2}$ at sweep rates up to 400 mV/s indicates that the electroactive species are diffusing clusters in solution and not films of clusters deposited on the electrode.[78]

Multi-electron-transfer reactions have been observed in small metal clusters previously, including Au_9 clusters protected by phosphines, and are typically thought to result as consequences of molecular rearrangements or solvation effects.[78,81,82] Contrary to the expectation that transfer of subsequent charges to a redox-active species becomes successively more difficult due to electrostatic repulsions, these effects make the second electron transfer to the electroactive species (reduction) or to the electrode (oxidation) thermodynamically more facile than the first electron transfer by virtue of the fact that the doubly reduced (or oxidized) species is more stable than the singly reduced (or oxidized) species.[78,79,81,82] This occurs due to solvation effects when the more highly reduced (oxidized) particle is more highly solvated.[78] Given the fact that the solvent used is methylene chloride, which should not exhibit preferential solvation dependent on the charge of the cluster, we favor an explanation in which there is a structural rearrangement in the cluster molecule. We note this latter property with some interest as

systems that can undergo such two-electron transfers could serve as potential catalysts for reactions requiring multielectron transfers, such as oxygen activation. Work is currently underway to better understand this interesting electrochemistry and its implications for gold catalysis.

Figure 5C presents the results from differential pulse voltammetry (DPV) studies of the second Au_{13} core cluster, compound **2**. This cluster exhibits similar behavior to **1** in that a large central gap is observed, but there are a number of obvious quantitative differences seen in the data. First, the electrochemical energy gap is smaller in energy (1.57 V, as measured between the first reduction peak (−1.73 V) and first oxidation peak (−0.16 V) in the oxidative DPV scan). This compares well with the gap measured optically (1.63 eV). Second, the first oxidation peak observed occurs at a lower potential than the first oxidation peak of the chlorinated analogue, a behavior consistent with the noted lability of **2** in an ambient atmosphere. Finally, the voltammetry does not show the sharp peaks observed for the chlorinated analogue. This smearing out of detail in the voltammetry is not believed to result from the presence of significant populations of larger clusters since the STEM measurements indicate that a very narrow distribution of cluster sizes is present in this case. The observed electrochemical behavior is more likely due to the fact that the ligands on **2** are not statically bonded to the gold core but show dynamical exchange, a fact that is fully supported by the data obtained by NMR spectroscopy.

For purposes of comparison, Figure 5D presents the results of electrochemical studies of the larger, fully thiolated MPCs. These voltammograms do not exhibit the redox chemistry of the molecule-like Au_{13} clusters. Rather, the voltammetry suggests a fairly large distribution of cluster core sizes, with broad charging peaks showing single-electron charging smeared out by the polydisperse nature of the sample.[24] The reaction and purification protocols presented in this work do not offer the rigorous control of cluster size for these fully thiolated clusters that is available for the Au_{13} clusters. Cyclic voltammograms are not presented for cluster **2** or for the fully thiolated MPCs because the features in these voltammograms are not sufficiently sharp to allow a precise determination of the cluster diffusion coefficients or the number of electrons transferred in the redox processes.

Near Infrared Luminescence. In addition to the UV−vis absorbance properties of the synthesized nanoparticles, their luminescent properties were also investigated. The near-IR luminescence of **1** was reported previously as part of a comparison to a number of larger gold nanoparticles.[83] The sub-nanometer clusters exhibit greater luminescence (higher quantum yields) than larger clusters as a result of their large energy level gaps, which decreases the contribution of nonradiative processes in relaxation.[84,85] Figure 6 displays the NIR photoluminescence spectra for **1**, **2**, and the thiolate-protected MPCs. The excitation wavelength used was 400 nm.

The quantum yields were measured with respect to DTTC and were determined to be 0.12, 0.055, and 8.6×10^{-4} for **1**, **2**, and the thiolate-protected MPCs, respectively. The quantum yields for **1** and **2** are of the same order of magnitude, which is not surprising given the similarities in their electronic structures. The magnitudes are consistent with those reported previously for **1**, but at the present no conclusion can be made as to whether the difference in quantum yield values for **1** and **2** results from experimental uncertainties (including the presence of some impurities in the samples) or from actual electronic effects resulting from the different properties of the two clusters.[83] Clusters protected with a monolayer of *n*-alkanethiolates that are similar in size to the thiolate-protected MPCs in this report have not exhibited significant luminescence in prior studies.[83] The weak luminescence observed in the present case is likely due to the existence of a small population of the small (e.g., Au_{13}) clusters in the sample. The estimate of the percentage of these small clusters in the sample from the quantitative STEM measurements is <2%, consistent with the very low value of the quantum yield found experimentally.

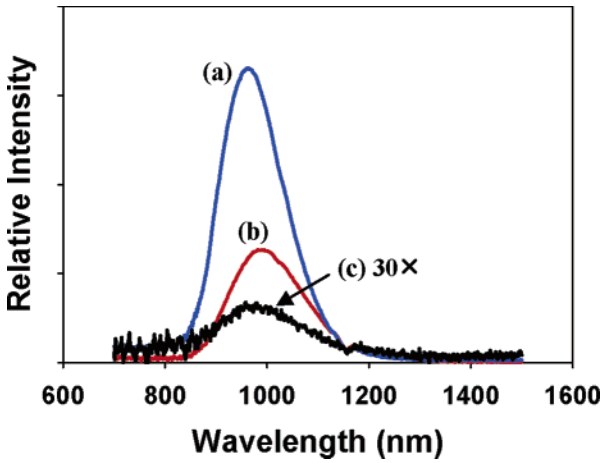

Figure 6. Near infrared emission spectra for (a) **1**, (b) **2**, and (c) thiol-protected MPCs. The quantum efficiencies (relative to DDTC) were determined to be 0.13, 0.055, and 8.6×10^{-4}, respectively.

Conclusions

The synthesis of 100 mg quantities of two slightly different Au_{13} cluster molecules ($Au_{13}[PPh_3]_4[S(CH_2)_{11}CH_3]_2Cl_2$ **(1)** and $Au_{13}[PPh_3]_4[S(CH_2)_{11}CH_3]_4$ **(2)**) is described. The atomic-scale characterization of the metal stoichiometries of these clusters at the single particle level is demonstrated using quantitative HAADF−STEM measurements that allow counting of the number of gold atoms in the cluster cores. Similar measurements on a sample of larger, thiolate-protected gold MPCs indicated a broad distribution of gold atom counts in the particle cores with an average core containing 183 gold atoms. The Au_{13} clusters show electronic properties that are distinct from the bulk metal and that vary based on changes in ligand composition. Additionally, the optical and electrochemical properties of the clusters **1** and **2**, in addition to being of fundamental interest, suggest a potential utility in catalytic systems. Further characterization of the sub-nanometer clusters using high-resolution electron microscopy and X-ray absorption spectroscopy have elucidated how these Au_{13} clusters exhibit structure not present in the bulk material; the sub-nanometer clusters are found to assume an icosahedral structure in contrast to the cubic phases characteristic of the bulk.[59]

Acknowledgment. This work was sponsored in part by grants from the Department of Energy (R.G.N., DEFG02-03ER15476; A.I.F., DEFG02-03ER15477; J.C.Y., DEFG02-03ER15475), the National Science Foundation (R.W.M.), and the Office of Naval Research (R.W.M.). Experiments were carried out at the Frederick Seitz Materials Research Laboratory at the University of Illinois at Urbana−Champaign, which is partially supported by the U. S. Department of Energy under grant DEFG02-91-ER45439. L.D.M. thanks the Office of the Deputy Undersecretary of Defense for Science and Technology and the Army Research Office for support through an NDSEG Fellowship.

Supporting Information Available: Selected area diffraction image of the masked dark-field detector and ^1H and ^{31}P-

{H} NMR spectra with a discussion of magnetic anisotropy effects and ligand dynamics apparent in the Au clusters. This material is available free of charge via the Internet at http://pubs.acs.org.

References and Notes

(1) *Nanoparticles: From Theory to Application*; Schmid, G., Ed.; Wiley-VCH: Weinheim, Germany, 2004.

(2) *Metal Nanoparticles: Synthesis, Characterization, and Applications*; Feldheim, D. L., Foss, C. A., Eds.; Marcel Dekker: New York, 2002.

(3) Templeton, A. C.; Wuelfing, W. P.; Murray, R. W. *Acc. Chem. Res.* **2000**, *33*, 27.

(4) Valden, M.; Lai, X.; Goodman, D. W. *Science* **1998**, *281*, 1647.

(5) Chen, S.; Ingram, R. S.; Hostetler, M. J.; Pietron, J. J.; Murray, R. W.; Schaaff, T. G.; Khoury, J. T.; Alvarez, M. M.; Whetten, R. L. *Science* **1998**, *280*, 2098.

(6) Schmid, G. *Chem. Rev.* **1992**, *92*, 1709.

(7) Hills, C. W.; Mack, N. H.; Nuzzo, R. G. *J. Phys. Chem. B* **2003**, *107*, 2626.

(8) Teo, B. K.; Shi, X.; Zhang, H. *J. Am. Chem. Soc.* **1992**, *114*, 2743.

(9) Hills, C. W.; Nashner, M. S.; Frenkel, A. I.; Shapley, J. R.; Nuzzo, R. G. *Langmuir* **1999**, *15*, 690.

(10) Yang, Y.; Chen, S. *Nano Lett.* **2003**, *3*, 75.

(11) Zhang, P.; Sham, T. K. *Appl. Phys. Lett.* **2002**, *81*, 736.

(12) Chao, K.-J.; Cheng, M.-H.; Ho, Y.-F.; Liu, P.-H. *Catal. Today* **2004**, *97*, 49.

(13) Haruta, M. *Catal. Today* **1997**, *36*, 153.

(14) Schaaff, T. G. *Anal. Chem.* **2004**, *76*, 6187.

(15) Brust, M.; Waker, M.; Bethell, D.; Schiffrin, D. J.; Whyman, R. *J. Chem. Soc., Chem. Commun.* **1994**, *7*, 801.

(16) Brust, M.; Fink, J.; Bethell, D.; Schiffrin, D. J.; Kiely, C. *J. Chem. Soc., Chem. Commun.* **1995**, *16*, 1655.

(17) Hostetler, M. J.; Wingate, J. E.; Zhong, C.-J.; Harris, J. E.; Vachet, R. W.; Clark, M. R.; Londono, J. D.; Green, S. J.; Stokes, J. J.; Wignall, G. D.; Glish, G. L.; Porter, M. D.; Evans, N. D.; Murray, R. W. *Langmuir* **1998**, *14*, 17.

(18) Zhong, C. J.; Zhang, W. X.; Leibowitz, F. L.; Eichelberger, H. H. *Chem. Commun.* **1999**, 1211.

(19) Maye, M. M.; Zheng, W.; Leibowitz, F. L.; Ly, N. K.; Zhong, C. J. *Langmuir* **2000**, *16*, 490.

(20) Shimizu, T.; Teranishi, T.; Hasegawa, S.; Miyake, M. *J. Phys. Chem. B* **2003**, *107*, 2719.

(21) Donkers, R. L.; Lee, D.; Murray, R. W. *Langmuir* **2004**, *20*, 1945.

(22) Brown, L. O.; Hutchison, J. E. *J. Am. Chem. Soc.* **1997**, *119*, 12384.

(23) Whetten, R. L.; Khoury, J. T.; Alvarez, M. M.; Murthy, S.; Vezmar, I.; Wang, Z. L.; Stephens, P. W.; Cleveland, C. L.; Luedtke, W. D.; Landman, U. *Adv. Mater.* **1996**, *8*, 428.

(24) Hicks, J. F.; Miles, D. T.; Murray, R. W. *J. Am. Chem. Soc.* **2002**, *124*, 13322.

(25) Warner, M. G.; Reed, S. M.; Hutchison, J. E. *Chem. Mater.* **2000**, *12*, 3316.

(26) Woehrle, G. H.; Warner, M. G.; Hutchison, J. E. *J. Phys. Chem. B* **2002**, *106*, 9979.

(27) Woehrle, G. H.; Brown, L. O.; Hutchison, J. E. *J. Am. Chem. Soc.* **2005**, *127*, 2172.

(28) Woehrle, G. H.; Hutchison, J. E. *Inorg. Chem.* **2005**, *44*, 6149.

(29) Mingos, D. M. P. *J. Chem. Soc., Dalton Trans.* **1996**, 561.

(30) Jaw, H.-R. C.; Mason, W. R. *Inorg. Chem.* **1991**, *30*, 3552.

(31) Bellon, P. L.; Cariati, F.; Manassero, M.; Naldini, L.; Sansoni, M. *J. Chem. Soc., Chem. Commun.* **1971**, 1423.

(32) Bellon, P. L.; Manassero, M.; Sansoni, M. *J. Chem. Soc., Dalton Trans.* **1972**, 1481.

(33) Briant, C. E.; Hall, K. P.; Wheeler, A. C.; Mingos, D. M. P. *J. Chem. Soc., Chem. Commun.* **1984**, 248.

(34) Schmid, G.; Pfeil, R.; Boese, R.; Brandermann, F.; Meyer, S.; Calis, G. H. M.; van der Velden, J. W. A. *Chem. Ber.* **1981**, *114*, 3634.

(35) Hostetler, M. J.; Templeton, A. C.; Murray, R. W. *Langmuir* **1999**, *15*, 3782.

(36) Wilcoxon, J. P.; Provencio, P. *J. Phys. Chem. B* **2003**, *107*, 12949.

(37) Balasubramanian, R.; Guo, R.; Mills, A. J.; Murray, R. W. *J. Am. Chem. Soc.* **2005**, *127*, 8126.

(38) Treacy, M. M. J.; Rice, S. B. *J. Microsc.* **1989**, *156*, 211.

(39) Singhal, A. Quantitative Electron Microscopy of Supported Sub-nanometer Clusters. Ph.D. Thesis, University of Illinois at Urbana−Champaign, Urbana, IL, 1996.

(40) Singhal, A.; Yang, J. C.; Gibson, J. M. *Ultramicroscopy* **1997**, *67*, 191.

(41) Yang, J. C.; Bradley, S.; Gibson, J. M. *Microsc. Microanal.* **2000**, *6*, 353.

(42) Yang, J. C.; Bradley, S.; Gibson, J. M. *Mater. Charact.* **2003**, *51*, 101.

(43) Smits, J. M. M.; Beurskens, P. T.; Bour, J. J.; Vollenbroek, F. A. *J. Cryst. Spectrosc.* **1983**, *13*, 365.

(44) Bellon, P.; Manassero, M.; Sansoni, M. *J. Chem. Soc., Dalton Trans.* **1973**, 2423.

(45) Schaaff, T. G.; Whetten, R. L. *J. Phys. Chem. B* **2000**, *104*, 2630.

(46) Zhang, H.-F.; Stender, M.; Zhang, R.; Wang, C.; Li, J.; Wang, L.-S. *J. Phys. Chem. B* **2004**, *108*, 12259.

(47) Schaaff, T. G.; Knight, G.; Shafigullin, M. N.; Borkman, R. F.; Whetten, R. L. *J. Phys. Chem. B* **1998**, *102*, 10643.

(48) Negishi, Y.; Nobusada, K.; Tsukuda, T. *J. Am. Chem. Soc.* **2005**, *127*, 5261.

(49) Liu, J. *Microsc. Microanal.* **2004**, *10*, 55.

(50) Williams, D. B.; Carter, C. B. *Transmission Electron Microscopy*; Plenum Press: New York, 1996.

(51) Jimenez, V. L.; Georganopoulou, D. G.; White, R. J.; Harper, A. S.; Mills, A. J.; Lee, D.; Murray, R. W. *Langmuir* **2004**, *20*, 6864.

(52) Keyse, R. J.; Garratt-Reed, A. J.; Goodhew, P. J.; Lorimer, G. W. *Introduction to Scanning Transmission Electron Microscopy*; Springer-Verlag: New York, 1998.

(53) Ibers, J. A.; Hamilton, W. C. *International Tables of X-ray Crystallography*; Kynoch Press: Birmingham, U. K., 1974.

(54) Schaaff, T. G.; Shafigullin, M. N.; Khoury, J. T.; Vezmar, I.; Whetten, R. L.; Cullen, W. G.; First, P. N.; Gutierrez-Wing, C.; Ascensio, J.; Jose-Yacaman, M. J. *J. Phys. Chem. B* **1997**, *101*, 7885.

(55) Wilcoxon, J. P.; Martin, J. E.; Provencio, P. *Langmuir* **2000**, *16*, 9912.

(56) Zharnikov, M.; Frey, S.; Heister, K.; Grunze, M. *Langmuir* **2000**, *16*, 2697.

(57) Heister, K.; Zharnikov, M.; Grunze, M. *Langmuir* **2001**, *17*, 8.

(58) Wagner, C. D.; Riggs, W. M.; Davis, L. E.; Moulder, J. F.; Muilenberg, G. E. E. *Handbook of X-ray Photoelectron Spectroscopy*; Perkin-Elmer Corporation: Eden Prairie, MN, 1979.

(59) Menard, L. D.; Xu, H.; Gao, S.-P.; Twesten, R. D.; Harper, A. S.; Song, Y.; Wang, G.; Douglas, A. D.; Yang, J. C.; Frenkel, A. I.; Murray, R. W.; Nuzzo, R. G. *J. Phys. Chem. B*, in press.

(60) Thomanny, A. L.; Braulty, P.; Rozenbaumy, J. P.; Andreazza-Vignollez, C.; Andreazzaz, P.; Estrade-Szwarckopfz, H.; Rousseauz, B.; Babonneaux, D.; Blondiauxk, G. *J. Phys. D: Appl. Phys.* **1997**, *30*, 3197.

(61) Chusuei, C. C.; Lai, X.; Luo, K.; Goodman, D. W. *Top. Catal.* **2001**, *14*, 71.

(62) Vollenbroek, F. A.; van den Berg, J. P.; van der Velden, J. W. A.; Bour, J. J. *Inorg. Chem.* **1980**, *19*, 2685.

(63) Schmid, G. *Struct. Bonding* **1985**, *62*, 51.

(64) Petroski, J.; Chou, M. H.; Creutz, C. *Inorg. Chem.* **2004**, *43*, 1597.

(65) Al-Somali, A. M.; Krueger, K. M.; Falkner, J. C.; Colvin, V. L. *Anal. Chem.* **2004**, *76*, 5903.

(66) Song, Y.; Jimenez, V. L.; McKinney, C.; Donkers, R. L.; Murray, R. W. *Anal. Chem.* **2003**, *75*, 5088.

(67) Song, Y.; Heien, M. L.; Jimenez, V. L.; Wightman, R. M.; Murray, R. W. *Anal. Chem.* **2004**, *76*, 4911.

(68) Jimenez, V. L.; Leopold, M. C.; Mazzitelli, C.; Jorgenson, J. W.; Murray, R. W. *Anal. Chem.* **2003**, *75*, 199.

(69) Link, S.; El-Sayed, M. A. *Int. Rev. Phys. Chem.* **2000**, *19*, 409.

(70) Hermann, M.; Kreibig, U.; Schmid, G. *Z. Phys. D* **1993**, *26*, S1.

(71) Hall, K. P.; Theobald, B. R. C.; Gilmour, D. I.; Mingos, M. P.; Welch, A. J. *J. Chem. Soc., Chem. Commun.* **1982**, 528.

(72) Bartlett, P. A.; Bauer, B.; Singer, S. J. *J. Am. Chem. Soc.* **1978**, *100*, 5085.

(73) Jahn, W. *J. Struct. Biol.* **1999**, *127*, 106.

(74) Benfield, R. E.; Maydwell, A. P.; van Ruitenbeek, J. M.; van Leeuwen, D. A. *Z. Phys. D* **1993**, *26*, S4.

(75) Lee, D.; Donkers, R. L.; Wang, G.; Harper, A. S.; Murray, R. W. *J. Am. Chem. Soc.* **2004**, *126*, 6193.

(76) Haram, S. K.; Quinn, B. M.; Bard, A. J. *J. Am. Chem. Soc.* **2001**, *123*, 8860.

(77) Lee, D.; Donkers, R. L.; DeSimone, J. M.; Murray, R. W. *J. Am. Chem. Soc.* **2003**, *125*, 1182.

(78) Bard, A. J.; Faulkner, L. R. *Electrochemical Methods: Fundamentals and Applications*; John Wiley & Sons: New York, 2001.

(79) van der Linden, J. G. M.; Paulissen, M. L. H.; Schmitz, J. E. J. *J. Am. Chem. Soc.* **1983**, *105*, 1903.

(80) Quinn, B. M.; Liljeroth, P.; Ruiz, V.; Laaksonen, T.; Kontturi, K. *J. Am. Chem. Soc.* **2003**, *125*, 6644.

(81) Evans, D. H. *Chem. Rev.* **1990**, *90*, 739.

(82) van der Linden, J. G. M.; Roelofsen, A. M.; Ipskamp, G. H. W. *Inorg. Chem.* **1989**, *28*, 967.

(83) Wang, G.; Huang, T.; Murray, R. W.; Menard, L.; Nuzzo, R. G. *J. Am. Chem. Soc.* **2005**, *127*, 812.

(84) Bigioni, T. P.; Whetten, R. L.; Dag, O. *J. Phys. Chem. B* **2000**, *104*, 6983.

(85) Dulkeith, E.; Niedereichholz, T.; Klar, T. A.; Feldmann, J.; von Plessen, G.; Gittins, D. I.; Mayya, K. S.; Caruso, F. *Phys. Rev. B* **2004**, *70*, 2054241.